Applied Thermal Engineering 223 (2023) 120011

Contents lists available at ScienceDirect

Applied Thermal Engineering

journal homepage: www.elsevier.com/locate/apthermeng

Research Paper

A numerical model coupling multiple heat transfer modes to develop a passive thermal management system for logging tool

Jiale Peng, Wei Lan, Fulong Wei, Chao Deng, Bin Xie, Xiaobing Luo *

School of Energy and Power Engineering, Huazhong University of Science and Technology, Wuhan, China

ARTICLE INFO

Keywords:
Logging tool
Numerical model
Passive thermal management
High temperature
Natural air convection
Thermal radiation

ABSTRACT

Logging tools are subjected to increasingly extreme thermal environments due to the exploration of deeper wells. Previous studies have shown that passive thermal management systems have successfully protected electronics that operate in high ambient temperature environments for up to several hours. However, the percentage of the contribution from different heat transfer modes remains unclear, and the numerical models remain incomplete. To solve this issue, a 3D numerical model that couples all heat transfer modes was proposed for passive thermal management systems of logging tool. Unlike previous simplistic models, the one proposed here considers solid heat conduction, natural air convection, thermal radiation, and the phase change heat storage processes. The accuracy of the proposed model was verified by experiments. The experimental results showed that the maximum absolute errors and the average absolute error between the simulation and experiment were 8.61 °C and 3.02 °C, respectively. The maximum percentage error between the experiment and simulation using the proposed model was 4.71 %, compared to 6.59 % for the previous model. Importantly, the heat transfer process was described in detail by numerical simulations. The results showed that the absorbed heat of the phase change materials accounted for 72.7 %, which suppressed the temperature rise of the heat sources. In addition, the proportions of thermal conduction, convection and radiation in the total heat exchange were 93.89 %, 4.32 %, and 1.79 %, respectively.

1. Introduction

As the global demand for petroleum resources increases and shallow oil and gas resources are exploited, the exploration of deeper and hotter wells becomes exceedingly attractive due to the economic and practical benefits [1-3]. However, according to geosphere researches, the downhole temperature rises 1–9 °C per 100 m, which suggests that downhole temperatures might exceed 200 °C [4]. Recently, an increasing number of high-temperature and high-pressure wells containing abundant petroleum resources have been discovered around the world. Hence, such a process for detecting underground petroleum resources requires the ability to operate in an extremely high temperature environment [5,6]. Logging tools play an important role in petroleum exploration. To detect reserves in high-temperature areas, the electronics inside the logging tool are forced to operate for hours at ambient temperature in excess of 200 °C. However, most standard electronics fail to withstand such a harsh environment since extremely high-temperature environment can lead to a decline of instrument reliability or even failure of the electronics [7,8].

To address this issue, numerous thermal management methods have been proposed including active and passive cooling techniques [9]. Various active cooling techniques, such as thermoelectric cooling [3,10-13], sorption cooling [14], vapor compression cycles [15-17] and liquid cooling [18], are able to achieve excellent cooling performance. However, these active cooling methods are not suitable for all logging applications due to the additional moving components, extra power input and low reliability. Hence, passive thermal management systems (PTMSs) for logging tools, which are composed of vacuum flasks, insulators, phase change materials (PCMs), electronics and skeleton, are attracting increasing attention due to their high reliability and integration [19]. A vacuum flask combined with insulators is applied to reduce heat transfer from a high-temperature environment. The PCMs between the skeleton and insulators are designed to absorb the heat generated from the electronics. Through the protection of a passive thermal management system, the electronics inside the logging tool can operate safely for hours in a high-temperature well [20].

The PTMSs for logging tools deployed at high ambient temperature possess a complex heat transfer process, which involves solid heat conduction, natural air convection, thermal radiation and solid-liquid

* Corresponding author.
E-mail address: luoxb@hust.edu.cn (X. Luo).

https://doi.org/10.1016/j.applthermaleng.2023.120011
Received 18 July 2022; Received in revised form 7 December 2022; Accepted 3 January 2023
Available online 6 January 2023

Nomenclature

ρ	Density
c	Specific heat capacity
k	Thermal conductivity
T	Temperature
t	Time
u	Air velocity
p	Air pressure
q	Power per unit volume
g	Gravity
μ	Air dynamic viscosity
J	Effective radiation
ε	Surface emissivity
σ	Stefan-Boltzmann constant
G	Input radiation
F	Radiation angle coefficient
θ	Emission angle
A	Surface area
R	Distance between the two surfaces
Q	Net radiation heat transfer
T_s	Initial phase change temperature of PCM
T_l	Final phase change end temperature of PCM
L_m	Latent heat
c_{eff}	Equivalent heat capacity of PCM
α	Volume fraction of liquid PCM
h_L	Average convective heat transfer coefficient
r_h	Radius of the wellbore wall
r_t	Radius of the logging tool
U	Velocity of the logging tool
L	Length of the logging tool
a	Thermal diffusion coefficient

Subscripts

0	Initial
air	Air
i	Surface i
j	Surface j
PCM-S	Solid PCM
PCM-L	Liquid PCM

phase change. In previous studies, several heat transfer models for PTMSs have been proposed to simulate the thermal performance under different condition. Initially, a 1D numerical PTMS model was proposed based on the energy conservation equation [21,22]. Through numerical calculation of the 1D nodes, the average temperature of nodes and the heat flow inside the logging tool were obtained. The 1D numerical model preliminarily explained the PTMS heat transfer process, whereas ignoring specific structures resulted in large discrepancies with the experimental results. With the development of numerical simulation, 2D numerical PTMS models were proposed to obtain the temperature contour of the logging tool, which further investigated the PTMS heat transfer process [23-25]. However, the actual structure of the logging tool is not symmetrical, and thus, the 2D numerical model possessed certain deficiencies in terms of heat transfer details, which failed to accurately describe the heat transfer process of the logging tool. To solve this issue, 3D numerical PTMS models that considers solid heat conduction and phase change processes were proposed [26-29]. The numerical results that were similar to the experimental results could be obtained, but the error was larger in the higher temperature interval due to the fact that that natural air convection and thermal radiation was neglected. Therefore, the 3D numerical models in previous studies were not sufficiently comprehensive. In addition, the proportion of heat conduction, natural air convection and thermal radiation in the PTMS remains unclear.

In this study, a 3D numerical PTMS model for the logging tool was proposed. The proposed model considers solid heat conduction, natural air convection, thermal radiation and phase change processes simultaneously (named as the SNTP numerical model). The SNTP numerical model was compared to the previous model with the same geometric model. The previous model only considers solid heat conduction and phase change processes (named as the SP numerical model). Additionally, an experiment was conducted to verify the accuracy of the SNTP numerical model. Finally, the transfer process was elucidated, and quantitative analyses of solid heat conduction, natural air convection, thermal radiation and phase change heat storage were carried out through numerical simulation.

2. Methods

2.1. Geometric model

Fig. 1 shows the geometric model (i.e., diagram) for the PTMS of a typical logging tool. A vacuum bottle is utilized to prevent radial heat transfer from the high-temperature downhole environment. The insulator 1 and 2 are located at the end of the vacuum bottle to block the axial environmental heat transfer. It is worth noting that there is a vacuum layer on the closed side of the vacuum bottle, but not on the open side. The space between the vacuum bottle and the metal skeleton is filled with air. Heat source 1 (20 W) and heat source 2 (10 W) are connected to the metal skeleton through thermal silicone pads. PCMs are applied for heat storage at both ends of the skeleton. Forced convection heat exchange occurs between the high temperature mud and the outer wall of the metal bottle during logging operation.

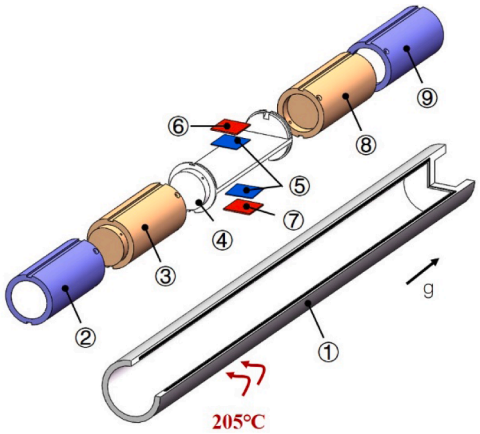

Fig. 1. Geometric PTMS model of a typical logging tool.

2.2. Numerical heat transfer model

In this section, the SNTP numerical model is described in detail. unlike previous simplistic models, the one proposed here considers solid heat conduction, natural air convection, thermal radiation and phase

change process inside the vacuum bottle. To simulate the transient heat transfer process efficiently and accurately, the following assumptions are made:

(1) The complex heat transfer process of the vacuum layer is equated to a solid heat transfer process with very low thermal conductivity [29].
(2) The effect of contact thermal resistance on heat transfer is ignored [20].
(3) The change in the physical properties of materials with respect to temperature is ignored [28].
(4) The electronics are treated as uniform heat sources.

The electronics inside the logging tool constantly generate heat during operation. Most of the heat is dissipated through the metal skeleton by solid heat conduction [30], which can be expressed as:

$$\rho c\frac{\partial T}{\partial t}=\nabla\cdot(k\nabla T)+q \tag{1}$$

Since air exists between the skeleton and the inner wall of the vacuum bottle, natural convection occurs within the closed cavity due to the temperature difference and gravity. In this study, the Boussinesq approximation is adopted to calculate the natural air convection in the closed cavity [31-33]. It is assumed that the air density change has no effect on the flow field, but affects the buoyancy force. The continuity equation can be simplified as:

$$\nabla\cdot\boldsymbol{u}=0 \tag{2}$$

The conservation of momentum equation for natural air convection [34] can be expressed as:

$$\rho_0\left(\frac{\partial \boldsymbol{u}}{\partial t}+\boldsymbol{u}\cdot\nabla\boldsymbol{u}\right)=-\nabla p+\mu\nabla^2\boldsymbol{u}+\rho_0\boldsymbol{g}-\rho_0\left(\frac{T-T_0}{T}\right)\boldsymbol{g} \tag{3}$$

The equation of energy conservation for natural convection can be expressed as:

$$\rho_{air}c_{air}\frac{\partial T}{\partial t}+\rho_{air}c_{air}\boldsymbol{u}\cdot\nabla T=\nabla\cdot(k_{air}\nabla T)+q \tag{4}$$

Since the air inside the vacuum bottle can be regarded as a radiation transparent medium, the radiant heat transfer that occurs among the skeleton, the heat source surface and the inner wall of the vacuum bottle can be calculated using the surface-to-surface radiation model. For surface i, the effective radiation can be expressed as:

$$J_i=(1-\varepsilon)G_i+\varepsilon\sigma T_i^4 \tag{5}$$

where G_i can be expressed as:

$$G_i=\sum_{j=1}^{N}F_{ij}J_j \tag{6}$$

where F_{ij} can be expressed as:

$$F_{ij}=\frac{1}{A_i}\int_{A_i}\int_{A_j}\frac{\cos\theta_i\cos\theta_j}{\pi R^2}dA_i dA_j \tag{7}$$

From Eq. (5)-(7), the radiation heat transfer of surface i can be expressed as:

$$Q_i=A_i\sum_{j=1}^{N}F_{ij}(J_i-J_j)=\sum_{j=1}^{N}\frac{J_i-J_j}{(A_iF_{ij})^{-1}} \tag{8}$$

Since the phase change involves a nonlinear process, it is calculated by the equivalent heat capacity method [35]. The equivalent heat capacity of PCMs can be expressed as:

$$c_{eff}=\begin{cases}c_{PCM-S} & (T<T_s)\\ \frac{1}{\rho}[(1-\alpha)\cdot\rho_{PCM-S}\cdot c_{PCM-S}+\alpha\cdot\rho_{PCM-L}\cdot c_{PCM-L}]+\frac{L_m}{T_l-T_s} & (T_s\leqslant T\leqslant T_l)\\ c_{PCM-L} & (T_l<T)\end{cases} \tag{9}$$

The equivalent density can be expressed as:

$$\rho_{PCM}=(1-\alpha)\cdot\rho_{PCM-S}+\alpha\cdot\rho_{PCM-L} \tag{10}$$

The equivalent thermal conductivity can be expressed as:

$$k_{PCM}=(1-\alpha)\cdot k_{PCM-S}+\alpha\cdot k_{PCM-L} \tag{11}$$

α is a function of temperature. It can be expressed as:

$$\alpha=\begin{cases}0 & (T<T_s)\\ \frac{V_{PCM-L}}{V_{PCM-L}+V_{PCM-S}} & (T_s\leqslant T\leqslant T_l)\\ 1 & (T_l<T)\end{cases} \tag{12}$$

Convective heat transfer between the metal vacuum bottle and the high temperature environment, and the average convective heat transfer coefficient can be expressed as [36].

$$h_L=\frac{1}{L}\int_0^L h(x)=\frac{3k_{mud}}{4}\left[\frac{U}{45(r_h-r_t)^2aL}\right]^{\frac{1}{3}}\left[(11r_h-5r_t)^{\frac{1}{3}}+\left(\frac{29r_h-5r_t}{16}\right)^{\frac{1}{3}}\right] \tag{13}$$

2.3. Simulated setup

In the simulation, COMSOL software was used to solve the numerical 3D model. The governing equations from the previous section were firstly added to the computational fluid dynamics (CFD) solver. Then, the 3D PTMS model for the logging tool was imported into the solver, and the unstructured tetrahedral mesh was divided. Subsequently, the materials and thermal properties of each component were defined as shown in Table 1. Notably, the vacuum layer of the metal vacuum bottle was equivalent to a solid layer with a thermal conductivity of 0.0002 W/(m·K) [29]. The phase change interval of the used PCM was 71.03–76.43 °C with a latent heat of 36.68 kJ/kg. The thermal expansion coefficient of the PCM was 6.47 × 10^{-5}/K [37]. The surface emissivity of the inner wall, skeleton, heat source, and insulator were 0.2, 0.16, 0.9 and 0.747 respectively [38-40]. Subsequently, the heating power of heat source 1 and heat source 2 were set to 20 W and 10 W, respectively. The external surface of the vacuum bottle was set as the convective heat transfer boundary condition with an ambient temperature of 205 °C. The initial temperature of the logging tool was set to 20 °C. Based on the transient CFD solver, the heat transfer process of the logging tool was calculated from 0 to 360 min with a time step of 10 min.

To ensure the accuracy of the calculated results, a grid-independence analysis was conducted. Numerical models with grid numbers of 50516, 77259, 148701 and 402411 were calculated. The calculated results are shown in Table 2. When considering the calculation error and computational resources, the numerical calculation results with grid number of 148701 were finally selected for the subsequent analysis with relative tolerance of 0.0001. In addition, to verify that the SNTP numerical model is more accurate than the SP numerical model, numerical simulations for the SP numerical model using the same geometric model were also performed.

2.4. Experimental setup

To verify the accuracy of the simulated results, the experimental measurements of the SNTP numerical PTMS model was conducted. As

Table 1
Materials and thermal properties of the logging tool [29,37-40].

Name	Material	Thermal conductivity ($W \cdot m^{-1} \cdot K^{-1}$)	Density ($kg \bullet m^{-3}$)	Heat capacity ($J \bullet kg^{-1} \bullet K^{-1}$)	Emissivity	Thermal expansion coefficient ($10^{-5}/K$)
Vacuum bottle	Inconel 718	14.7	8240	436	0.2	\
Vacuum layer	Composite	0.0002	100	1200	\	\
Skeleton	Aluminum alloy 6061	167	2710	896	0.16	\
Heat sources	Ceramic	30	3960	850	0.9	\
PCM	Wood alloy	19.8	9657.9	166.7(s)184(l)	\	6.47
Insulator shell	PTFE	0.25	2200	1000	0.747	\
Insulator core	Aluminum Silicate wool	0.035	400	794.2	\	\

Table 2
Grid independent analysis.

Grid number	Temperature of heat source 1 (°C)	Grid number	Temperature of heat source 1 (°C)
50516	162.18	148701	159.15
77259	160.61	402411	159.34

shown in the Fig. 2(a), a skeleton prototype of the logging tool with the PTMS was fabricated on a scale of one to one with the simulated model. The two ceramic heating elements(40 mm × 40 mm × 2 mm, 10 W/5 V or 20 W/12 V, Zhengzhou Xindeng Electrothermal Ceramics Ltd.), were adhered to the skeleton by thermal silicone pads(LC120,1W/(m·K), Shenzhen Liantengda Technology Ltd.). The contact surfaces are filled with thermal interface material to reduce the contact thermal resistance. Subsequently, thermocouples (K type, 2 × 0.3 mm, Shenzhen Yibulan Electronics Ltd.) were positioned at several temperature measurement points, such as at the heat sources, insulators and PCMs, as shown in Fig. 2(a). The metal vacuum bottle (JP90/73 × 900, Xi'an Yufeng Electronics Company Ltd.) was utilized to contain the prototype with heat sources and thermocouples. Then, the metal vacuum bottle with the prototype was put into the oven (DHG-9205A, temperature range 10–300 °C, accuracy ± 0.5 °C, Shanghai Hecheng Instrument Manufacturing Ltd), as shown in Fig. 2(b). In addition, adjustable DC voltage regulators (MS-3010D, 0–30 V/10 A, Dongguan Meisheng Power Technology Ltd.) were implemented to supply power to the ceramic heating elements. A data acquisition instrument (MIK-R6000F, temperature measurement accuracy 0.2 % FS ± 1 D, sampling frequency 1 Hz, Hangzhou Mecon Automation Technology Ltd.) was used to collect and deal with temperature measurement signals. Finally, the oven temperature was controlled by a PID controller to maintain a temperature of 205 °C for 6 h.

3. Results and discussion

3.1. Experimental results

Fig. 3 shows the comparison of the experimental temperatures and simulated temperatures of the PTMS. The temperatures of heat source 1, heat source 2, PCM 1, PCM 2, and insulator 2 are selected to compare the numerical and experimental results. The experimental temperatures show the same trends as the simulated temperature. During the whole process, the maximum absolute errors between the measured and simulated temperatures of heat source 1, heat source 2, PCM 1, PCM 2 and insulator 2 were 5.39 °C, 5.41 °C, 8.52 °C, 9.43 °C and 3.78 °C, respectively. The maximum absolute errors were within 10 °C, and the

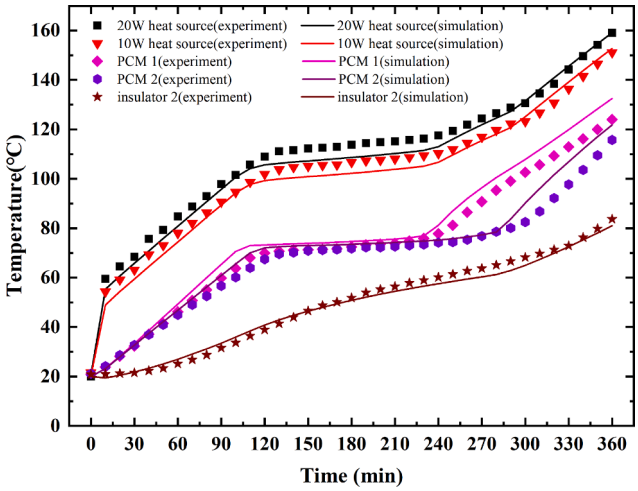

Fig. 3. Comparison of the simulated and experimental temperatures of the PTMS.

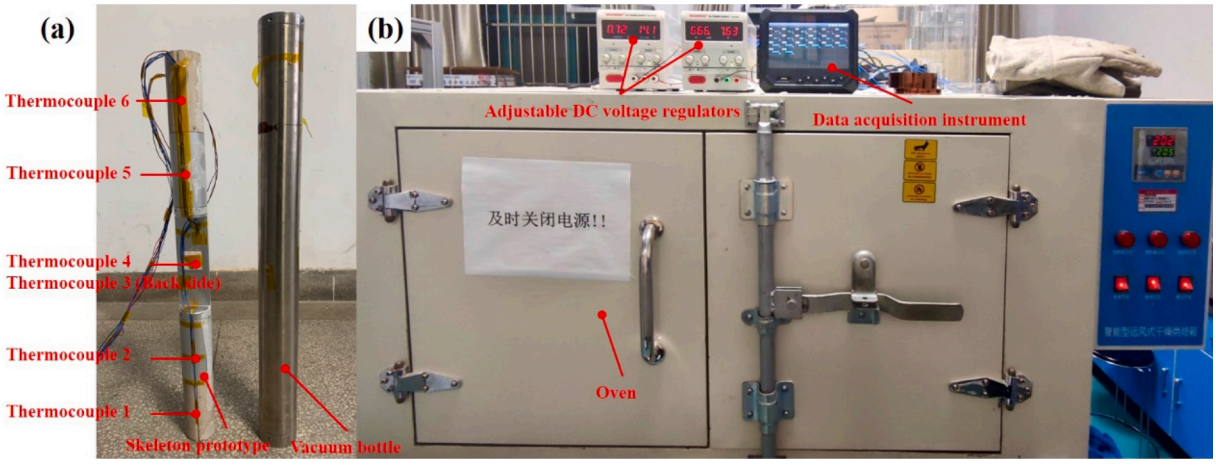

Fig. 2. Experimental test: (a) Skeleton prototype of the typical logging tool and the metal vacuum bottle; (b) high-temperature oven temperature test site.

average absolute error was only 3.02 °C, which demonstrated the accuracy of the simulated results.

The errors between the experiment and simulation mainly originated from the assumptions regarding the numerical simulations and the experiment setup. First, the contact thermal resistance was neglected in the simulation, which reduced the heat transfer thermal resistance between the heat sources and PCMs. Therefore, the simulated temperatures of the heat sources were generally lower than the experimental temperature during the 290 min operation, while the simulated temperature of the PCMs was higher than the experiment temperature. In addition, the contact thermal resistance delayed the onset of the phase transition of the PCMs in the experiment. Since the contact surfaces in the experiment were filled with thermal interface material, the error was within the accepted range. Second, the error originated from the assumption that the change in physical properties of materials with temperature was ignored. When the temperature was higher, the material properties deviated from the defined properties at room temperature. Therefore, the heating rate of the heat sources and PCMs in the simulation was different from that in the experiment after 290 min. The change of material properties with temperature had minor effect on the overall system. Finally, the experiment tests also introduced several errors. On the one hand, the experimental error derived from the temperature collection accuracy of the equipment, which was ± 0.7 °C in this study. On the other hand, the ambient temperature in the experiment gradually rose from room temperature to 205 °C, while the simulation was directly set to the ambient convective heat transfer temperature of 205 °C. These differences had a small effect on the internal temperature rise due to the excellent insulation of the vacuum bottle and the insulator. Overall, the errors between the experimental results and the simulated results were within acceptable limits.

3.2. Comparison with previous numerical model

Fig. 4 shows the heat source temperature timeseries for different numerical PTMS models. The SP numerical model only considers solid heat conduction and phase change. The temperature curves of the proposed numerical model were closer to the experimental results than those of the SP numerical model. The simulated results of SP numerical model were not much different from that of SNTP numerical model before 210 min. However, the temperature difference between them gradually increased due to the enhancement of thermal convection and radiation after 210 min. Overall, the heat source temperature difference between the simulated results of the SP numerical model and the experimental results reached a maximum absolute error of 8.61 °C, while the maximum error between the simulated results of the SNTP numerical model and the experimental test results was within 6 °C. The maximum percentage error between the experiment and simulation in the SNTP numerical model was 4.71 %, compared to 6.59 % in the SP numerical model. As a result, the SNTP numerical model accurately characterized the real heat transfer process in the logging tool. In addition, the computation times of the SP numerical model and the SNTP numerical model were 635 s and 29296 s, respectively.

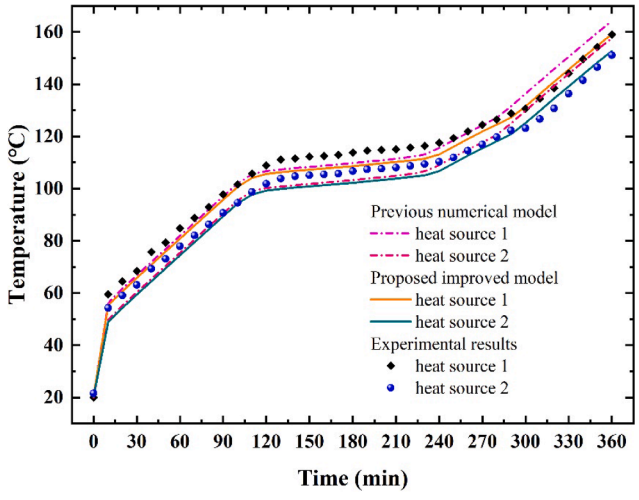

Fig. 4. The heat source temperature timeseries for different numerical PTMS models.

3.3. Temperature field

Fig. 5 shows the temperature distribution of the SNTP numerical model towards PTMS at different time intervals. The temperature of the PTMS increased with time due to the combined effect of operating within a high-temperature environment and self-generated heat. Since the opening of the vacuum bottle was in direct contact with the external high-temperature environment, insulator 1 displayed a large temperature gradient and the heat from environment continuously penetrated into the interior of the vacuum bottle. However, insulator 2 was near the closed side of the vacuum bottle, which was less affected by the high-temperature environment, leading to its lower temperature. Due to the accumulation of the generated heat, the heat source temperature was generally higher than that of the metal skeleton and the nearby PCM. The maximum temperature of the heat sources reached 159.15 °C after 6 h. In addition, the PCMs underwent a phase change process during the 2 to 4 h interval, and their temperature remained constant near the melting point. Therefore, the overall temperature field of PTMS remained almost the same during the 2 to 4 h interval, reflecting the significant effect of the PCMs' latent heat on the temperature control.

Fig. 6 shows the temperature curves of the logging tool over time. Influenced by the generated heat, the temperature of heat source 1 rose rapidly to approximately 50 °C in the first stage, resulting in a certain temperature difference with the PCMs. In the second stage, it rose at a uniform rate of 30.4 °C/h due to the sensible heat of the metal skeleton and the PCMs. In the third stage, PCM 1 and PCM 2 finished the phase change process and absorbed excessive heat from the heat sources in the form of latent heat. The temperature of the heat sources remained almost constant between 100 and 280 min. In the fourth stage, the PCMs continued to absorb heat in the form of sensible heat, thus leading to the temperature rise of the heat sources at a rate of 25.97 °C/h.

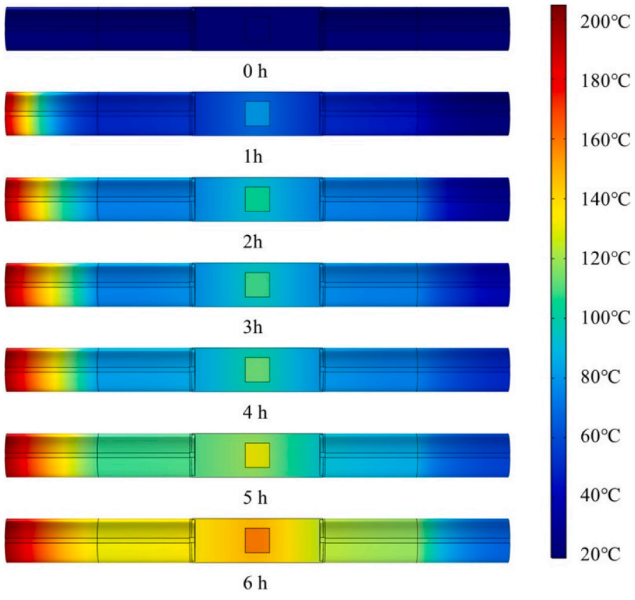

Fig. 5. Temperature distribution of the PTMS for a typical logging tool.

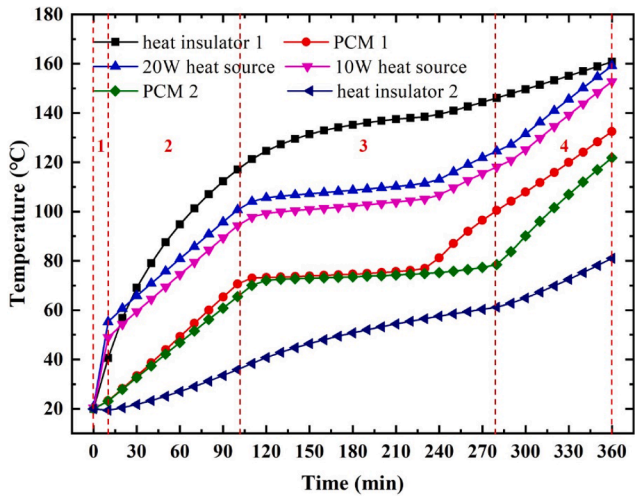

Fig. 6. Temperature curves of the logging tool versus time.

3.4. Flow field

Fig. 7 depicts the air flow near the heat source inside the vacuum bottle. The direction of the red arrows indicates the direction of the natural air convection. The size of the arrow indicates the magnitude of the air velocity. The colors of the heat sources and the metal skeleton denote the temperature. The temperature of the air near the heat sources is higher and has a lower density than the air flow inside the logging wool. The air moves upward due to the combined effect of the temperature gradient and gravity and is then dispersed in all directions after encountering the barrier imposed by PCM 1. In addition, the lower temperature of the inner vacuum bottle wall contributed to the cooling of the nearby air, which resulted in a downward return flow.

Fig. 8 shows the velocity distribution of the air inside the vacuum bottle, where the arrows indicate the direction of the air flow and the colors reflect the magnitude of the velocity. At the beginning, there was no temperature difference inside the vacuum bottle, and the air was stationary. The air flowed upward due to the change in density after 1 h, and it descend due to the cooling of the inner wall of the vacuum bottle. Two vortices were clearly visible near the heat source. The flow field from 2 to 4 h was approximately the same as that at 1 h. The minor difference was that two new small reverse vortices appeared below the metal skeleton near the inner wall of the vacuum bottle. The temperature of PCM 2 was lower than that of the nearby vacuum bottle wall due to the phase change of PCM 2, and thus two small reverse vortices appeared on account of the temperature difference. The temperature of the metal skeleton further climbed again from 5 to 6 h due to the end of the phase transition, which was higher than that of the nearby wall of the vacuum bottle. Hence, the small reverse vortices disappeared. Overall, the natural air convection velocity inside the vacuum bottle ranges from 0 to 0.1 m/s. The air between the PCMs and the vacuum bottle is nearly stationary. The natural convection of air inside the vacuum bottle accelerates the dissipation of the heat from the heat sources.

3.5. Phase change heat storage

As the main heat storage pool of PTMS, PCMs are crucial for the temperature control of the heat source. Therefore, it is necessary to analyze the phase change process of PCMs. Fig. 9(a) shows the phase change of the PCMs over time, where 0 and 100 % indicate the solid PCM and the liquid PCM, respectively. 0–100 % indicate the solid–liquid mixing area of PCM, which reflects the phase change interface. The PCMs were solid from 0 to 1 h, as shown in Fig. 9(a). The phase change process started from the sides nearest the heat source at approximately 2 h and then gradually advanced towards the two ends of the logging instruments until 5 h, at which time the phase change was complete. The generated heat from the heat sources was the main reason for the phase change process. The extreme ambient temperatures had less effect on internal phase changes due to the superior thermal insulation of the vacuum bottle and insulators. In addition, PCM 1 completed the phase change process approximately 1 h earlier than PCM 2 due to the influence of the high-temperature environment.

Fig. 9(b) displays the fraction of liquid PCMs curves as a percentage of volume over time. The x-axis is the time, and the y-axis is the percentage of the liquid PCM volume (0–100 %). Both PCM 1 and PCM 2 started the phase transition process at approximately 100 min. Since PCM 1 was located at the open side of the vacuum bottle, the phase transition of PCM 1 was completed at 240 min. The phase transition time of PCM 2 was relatively slower, and the phase transition completed at 290 min. Since the phase transition process of PCM 1 was not synchronized with that of PCM 2, the total PCMs phase transition trend was significantly altered by the time the phase change of PCM 1 was

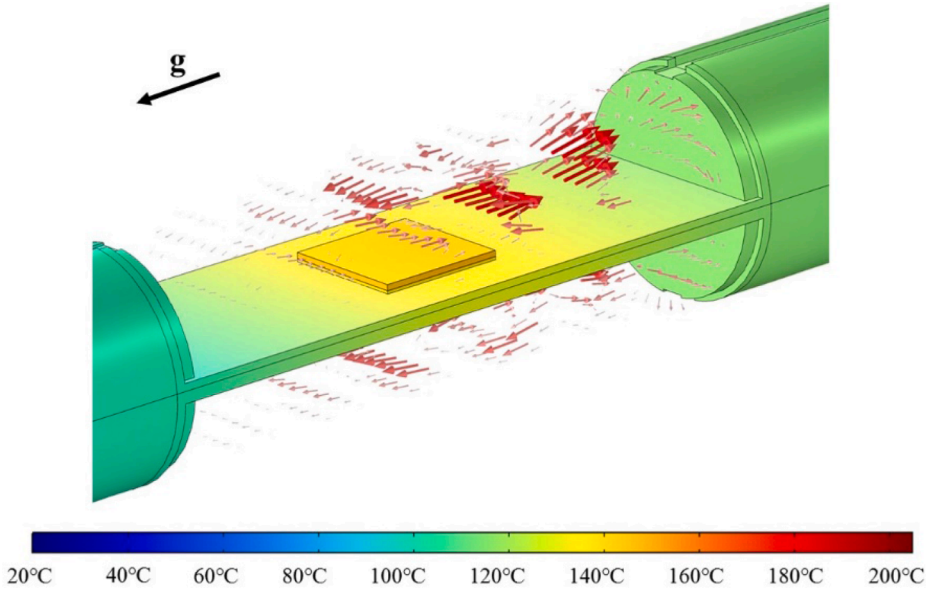

Fig. 7. The air flow near the heat source in the vacuum bottle.

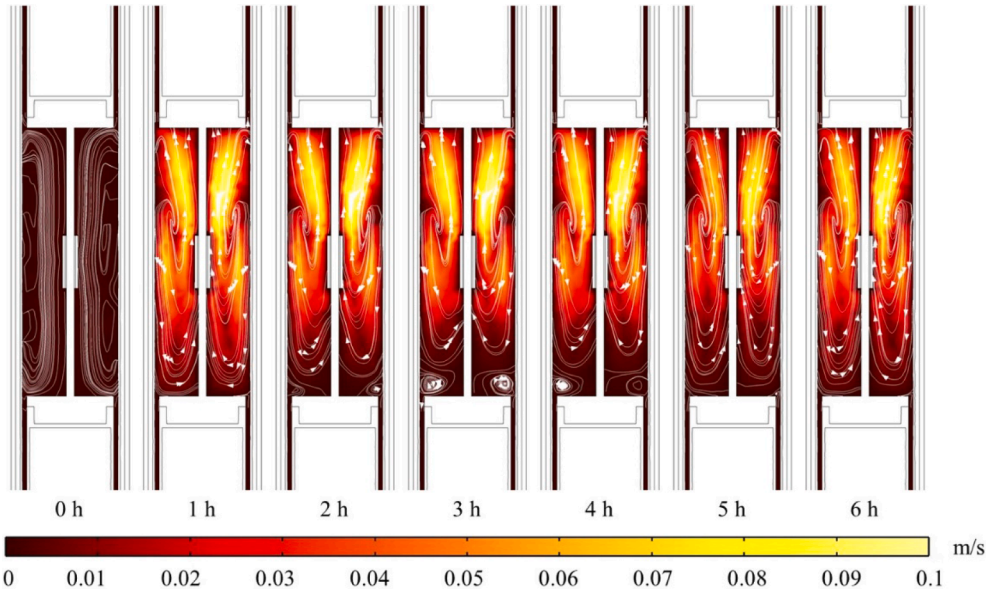

Fig. 8. The velocity distribution of the air inside the vacuum bottle.

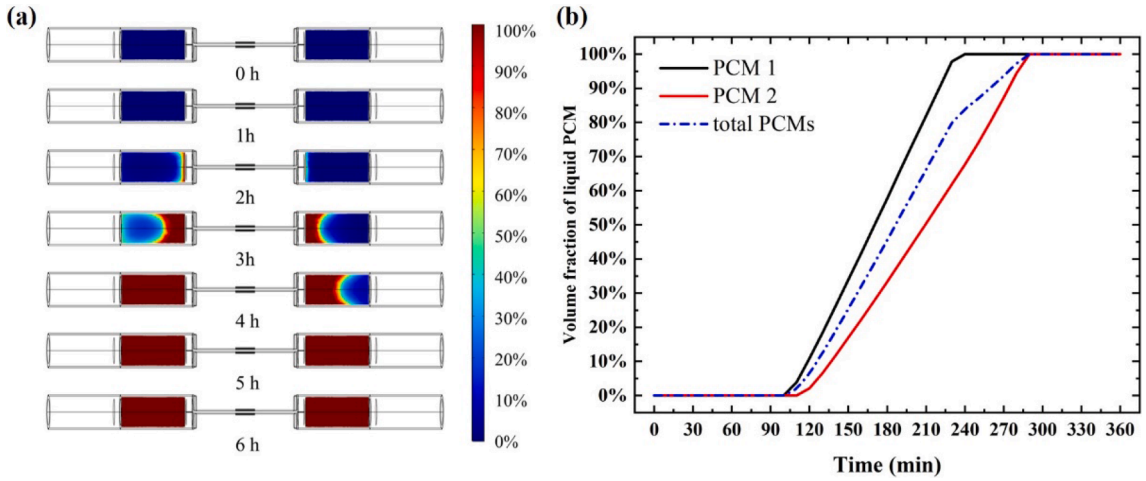

Fig. 9. PCM phase transition (a) Phase transition of PCMs within the logging tool at one hour intervals (b) Liquid PCMs as a percentage of volume versus time.

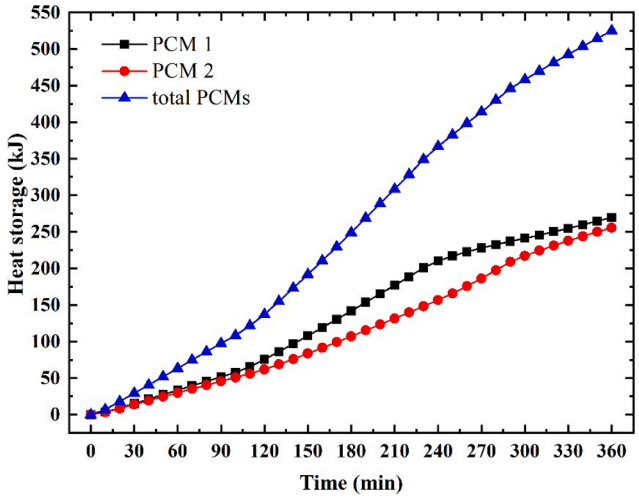

Fig. 10. PCM heat storage timeseries.

completed.

The heat storage of the PCMs is further shown in Fig. 10. When the PCMs were pure solid or pure liquid, the PCMs only accumulated heat in the form of sensible heat with a lower heat storage rate. When the PCMs were under the melt phase transition, their temperature was maintained near the melting point for a longer period of time, which showed a great heat storage effect and kept the temperature of other components from rising. Therefore, the PCM heat storage timeseries showed two inflection points, which represented the beginning and end of the phase change, and the slope of the curves between the two inflection points was significantly larger. The total heat storage of the PCMs reached 525.354 kJ (the absorbed heat of PCM 1 and PCM2 were 269.654 kJ and 255.700 kJ, respectively). Among them, latent heat storage accounted for 58.1 %, which played a significant role in the whole heat storage process of PCMs.

3.6. Heat flow

Fig. 11(a) shows final the temperature distribution and heat flow of PTMS, where the color indicates the temperature and the red arrows indicate the direction and size of the heat flow. The great majority of

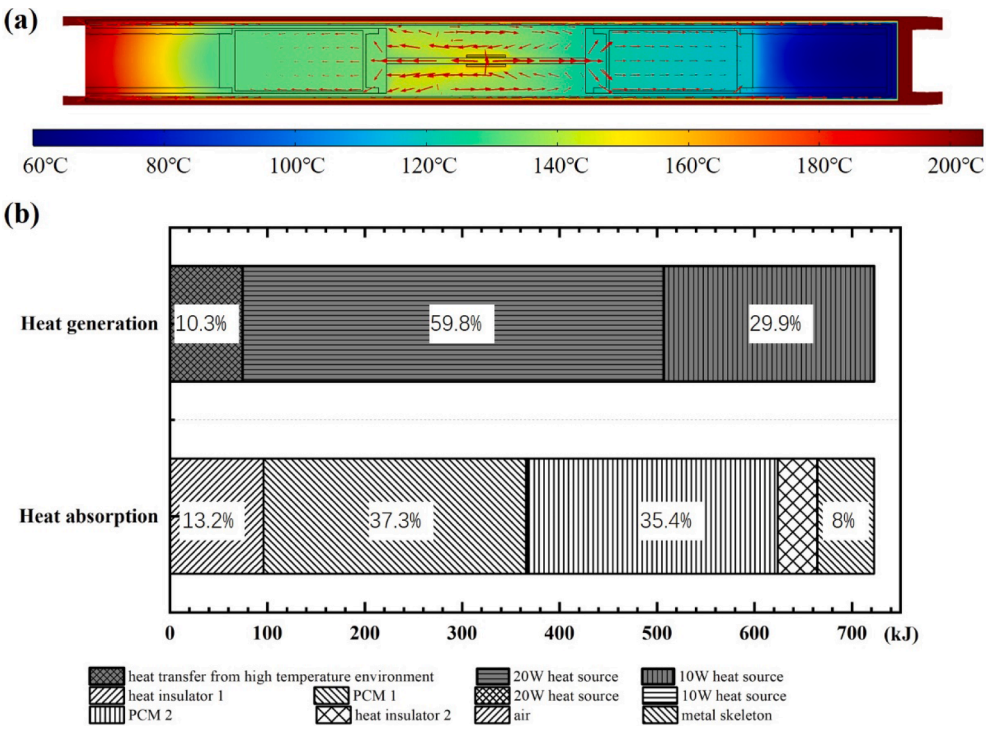

Fig. 11. Heat flow distribution, heat generation and absorption (a) The final temperature and heat flow distribution of PTMS (b) Analysis of the heat generation and heat absorption of the PTMS.

heat from the heat sources was dissipated to the metal skeleton through the thermal silicone pad, and then transferred to the PCMs along the skeleton to the left and right. At the junction of the metal skeleton and the PCMs, there was a significant heat diffusion process due to the change in cross-sectional area. After the heat flow entered the interior of the PCMs, it decreased, which visually reflected the heat storage process offered by the PCMs. Concerning the heat exchange by natural convection of air, the direction of heat flow was consistent with the velocity of air movement, which illustrated that the macroscopic movement of air could strengthen the heat exchange process. In addition, due to the outstanding thermal insulation of the vacuum layer, there was a "thermal bridge effect" at the opening of the vacuum bottle [41]. The heat from the external high-temperature environment could bypass the vacuum layer and seep into the interior of the vacuum bottle, which further intensified the environmental heat transfer at the opening of the vacuum bottle.

The heat generation and absorption capacities of the PTMS are further quantified, as shown in Fig. 11(b). First, the heat generation was mainly divided into two parts: heat generated from the heat sources and heat transfer from the high-temperature environment. Among them, the heat transfer from the high-temperature environment reached 74.67 kJ, which only accounted for 10.3 % of the total heat. The heat sources constantly generated a total 648 kJ of heat during the 6 h of operation, which accounted for 89.7 % of the total heat. Since the heat cannot be dissipated to the high-temperature environment, all the heat was absorbed by each component of the PTMS, resulting in an increase in the overall enthalpy and temperature. PCM 1 and PCM 2 possessed abundant heat storage capacity, which accounted for 37.3 % and 35.4 % of the total heat storage, respectively, reflecting the essential role of PCMs in the PTMS. The PCMs were the most significant heat storage component of the logging tool when subjected to high ambient temperatures. The metal skeleton, insulator 1 and insulator 2 absorbed 8 %, 13.2 % and 5.6 % of the heat in the form of sensible heat, respectively. In addition, part of the heat was still trapped in heat source 1 and heat source 2, which was 1382.7 J and 1320.4 J, respectively, and caused their temperature to rise.

The heat source temperature is a key indicator of the PTMS for the logging tool. The final temperature is tightly related to the heat dissipation capability. Therefore, it is necessary to focus on the heat dissipation path of the heat sources. Fig. 12 displays the heat dissipation paths of heat source 1 and heat source 2. The majority of the generated heat from the heat sources was transferred to other components via heat conduction, natural air convection and thermal radiation, and only 0.47 % and 0.86 % of the total heat was trapped within heat source 1 and heat source 2, respectively. Among the three forms of heat transfer, thermal conduction played a dominant role, where 94.0 % of heat source 1 and 92.5 % of heat source 2 was dissipated through the metal skeleton. Overall, the proportions of solid heat conduction, natural air convection and thermal radiation heat exchange are 93.89 %, 4.32 %, and 1.79 %, respectively, which reflects the absolute dominance of solid heat conduction in the whole heat exchange process.

4. Conclusions

We proposed a numerical model that coupled multiple heat transfer modes to create a passive thermal management system for logging tools. The proposed model considers solid heat conduction, natural air convection, thermal radiation, and phase change processes simultaneously. The experimental results showed that the maximum absolute error between simulation and experiment was 8.61 °C, and the average absolute error was only 3.02 °C, thus demonstrating the accuracy of the numerical model. The proposed model can characterize the real heat transfer process accurately with a deviation of 4.71 % from the experiment. It is noted that the computation time of the proposed improved model is long, and better methods should be proposed in future work to reduce the computation time while ensuring computational accuracy.

Declaration of Competing Interest

The authors declare that they have no known competing financial interests or personal relationships that could have appeared to influence the work reported in this paper.

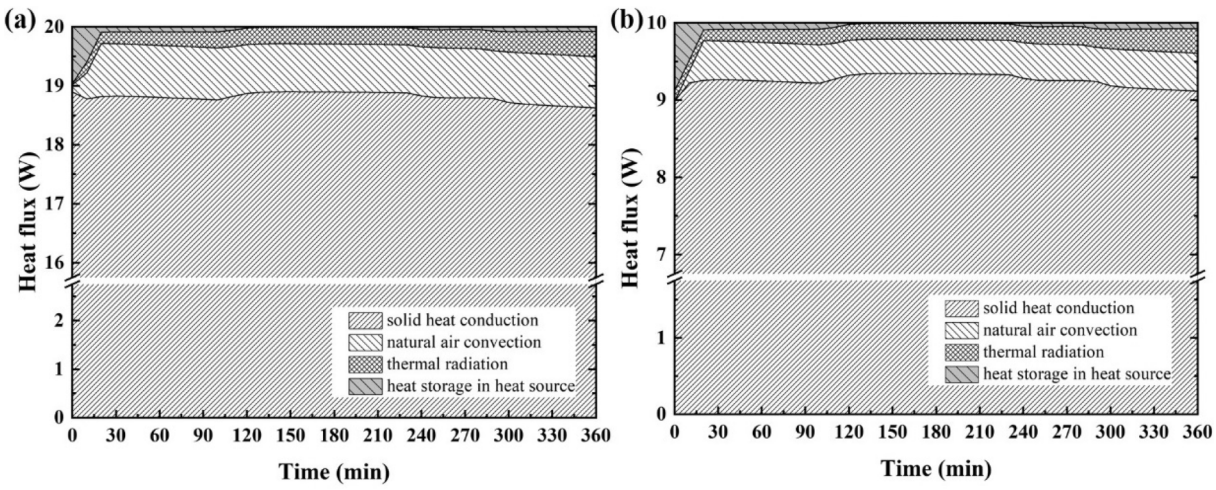

Fig. 12. Heat dissipation path analysis (a) heat source 1 (b) heat source 2.

Data availability

Data will be made available on request.

Acknowledgement

This research is supported by the National Natural Science Foundation of China (51625601).

Appendix A. Supplementary material

Supplementary data to this article can be found online at https://doi.org/10.1016/j.applthermaleng.2023.120011.

References

[1] A. Shadravan, M. Amani. HPHT 101 - what every engineer or geoscientist should know about high pressure high temperature wells. in: SPE Kuwait International Petroleum Conference and Exhibition. Dec. 2012, 1-27.
[2] L.J. Bernard, S. Dyer, A. Harrison, M. Arena, W. Luckett, Testing oilfield technologies for wellsite operations, Oilfield Review 17 (4) (2005) 58–67.
[3] S. Soprani, A.J. Nørgaard, C. Nesgaard, K. Engelbrecht, Design and testing of a heat transfer sensor for well exploration tools, Appl. Therm. Eng. 141 (2018) 887–897.
[4] N.J. Hyne, Nontechnical guide to petroleum geology. Exploration, Drilling & Production, (3rd ed)., AAPG, Boulder, Tulsa, USA, 2012.
[5] J. Boyes, The eyes of the oil industry, Electron. Power 27 (6) (1981) 484–488.
[6] T. Baird, T. Fields, R. Drummond, D. Mathison, L. Silipigno, High-pressure, high-temperature well logging, perforating and testing, Oilfield Review 10 (2) (1998) 50–67.
[7] C. Buttay, D. Planson,B Allard, D. Bergogne, P. Bevilacqua, C. Joubert, M. Lazar, C. Martin, H. Morel, D. Tournier. State of the art of high temperature power electronics, Materials Science and Engineering: B, 176(4) (2011) 283-288.
[8] J. He, Q. Wang, J. Wu, Y. Zhang, W. Chu, Hybrid thermal management strategy with PCM and insulation materials for pulsed-power source controller in extreme oil-well thermal environment, Appl. Therm. Eng. 214 (2022), 118864.
[9] Y. Lv, W. Chu, Q. Wang, Thermal management systems for electronics using in deep downhole environment: A review, Int. Commun. Heat Mass Transfer 139 (2022), 106450.
[10] A. Sinha, Y. Joshi. Application of thermoelectric-adsorption cooler for harsh environment electronics under varying heat load. Journal of Thermal Science and Engineering Applications. 2(2) (2010) 021004-1-021004-9.
[11] W. Gao, K. Liu, X. Dou, L. Zhang, S. Tang, Numerical investigation on heat transfer rate from the outside environment into the electronic compartment of the measurement-while-drilling tools, Heat Transfer 50 (6) (2021) 5835–5852.
[12] W. Gao, K. Liu, X. Dou, S. Tang, L. Zhang, Numerical investigation on cooling effect in the circuit cabin of active cooling system of measurement-while-drilling instrument based on split-Stirling retrigerator, Case Stud. Therm. Eng. 28 (2012), 101621.
[13] R. Weerasinghe, T. Hughes, Analysis of thermal performance of geophonic downhole measuring tools; a numerical and experimental investigation, Appl. Therm. Eng. 137 (2018) 504–512.
[14] E. Pennewitz, T. Kruspe, S. Jung, M. Schilling, Evaluation of sorbents at elevated temperatures for downhole application, Chem. Eng. Trans. (2012) 1543–1548.
[15] Q. E. S. Verma. Thermal management of electronics used in downhole tools. In: SPE Annual Technical Conference and Exhibition, Oct. 2012: SPE-159737-MS.
[16] H.J.I. Benedict, Cooling systems for borehole tools, J. Geol. Resour. Eng. 1 (2013) 55–60.
[17] H.J.I. Benedict, Development of a cooling system for geothermal borehole probes, J. Earth Sci. Eng. 4 (2) (2013) 73–79.
[18] J. Jakaboski, Innovative thermal management of electronics used in oil well logging, Georgia Institute of Technology, Georgia, 2004.
[19] B. Shang, Y. Ma, R. Hu, C. Yuan, J. Hu, X. Luo, Passive thermal management system for downhole electronics in harsh thermal environments, Appl. Therm. Eng. 118 (2017) 593–599.
[20] J. Zhang, W. Lan, C. Deng, F. Wei, X. Luo, Thermal Optimization of High-Temperature Downhole Electronic Devices, IEEE Trans. Compon. Packag. Manuf. Technol. 11 (2021) 1816–1823.
[21] B. Holbein, J. Isele, L. Spatafora, Integrated cooling systems for an extended operation range of borehole tools, Geotherm. Resour. Council Trans. 39 (2015) 1073–1078.
[22] S. Rafie, Thermal management of downhole oil and gas logging sensors for HTHP applications using nanoporous materials. In: Proceedings of 2nd Energy Nanotechnology International Conference. Sept, 2007.
[23] G.A. Bennett, G.R. Sherman, Analysis and thermal-design improvements of downhole tools for use in hot-dry wells, Los Alamos National Laboratory, New Mexico, 1983.
[24] X. Zhang, C. An, J. Zhang, Y. Zhang. Analysis of heat transfer performance of insulation casing filled with phase change material for downhole instruments. In: 30th International Ocean and Polar Engineering Conference. Oct. 2020, OnePetro, 3120-3124.
[25] Z. Xue, B. Shang, J. Zhang, et al., Numerical Simulation Analysis of Thermal Management System of High Temperature Well Logging Tool, Drill. Prod. Technol. 44 (5) (2021) 92–96.
[26] J.R. Sisler, S.J. Zarrouk, R. Adams, Improving Down-Hole Working Time of PTS Probes Used in Geothermal Wells, Geotherm. Resour. Council Trans. 38 (2015) 563–567.
[27] A. Sur, B. Kouchmeshky, R. Satti. Thermal modeling of a wireline tool for ultra-high temperatures. In: Proceedings of the ASME 2014 4th Joint US-European Fluids Engineering Division Summer Meeting. Aug. 2014, ASME, 2014, 21851.
[28] W. Lan, J. Zhang, J. Peng, Y. Ma, S. Zhou, X. Luo, Distributed thermal management system for downhole electronics at high temperature, Appl. Therm. Eng. 180 (2020), 115853.
[29] J. Peng, W. Lan, Y. Wang, Y. Ma, and X. Luo. Thermal management of the high-power electronics in high temperature downhole environment, In: Proceedings of IEEE 22nd Electronics Packaging Technology Conference *(EPTC)*, Dec. 2020, 369–375.
[30] J.P. Holman, Heat transfer (10th Edition), McGraw Hill Education, New York, 2009.
[31] D.D. Gray, A. Giorgini, The validity of the boussinesq approximation for liquids and gases, Int. J. Heat Mass Transf. 19 (5) (1976) 545–551.
[32] H.M. Blackburn, J.M. Lopez, J. Singh, A.J. Smits, On the Boussinesq approximation in arbitrarily accelerating frames of reference, J. Fluid Mech. 924 (1) (2021) 1–11.
[33] D.V. Lyubimov, T.P. Lyubimova, J.I.D. Alexander, N.I. Lobov, On the boussinesq approximation for fluid systems with deformable interfaces, Adv. Space Res. 22 (8) (1998) 1159–1168.
[34] P. Mayeli, G.J. Sheard, Buoyancy-driven flows beyond the Boussinesq approximation: A brief review, Int. Commun. Heat Mass Transfer 125 (2021), 105316.
[35] Y. Hu, R. Guo, P.K. Heiselberg, H. Johra, Modeling PCM phase change temperature and hysteresis in ventilation cooling and heating applications, Energies 13 (23) (2020) 6455.
[36] A.G. Flores, Active cooling for electronics in a wireline oil-exploration tool, Massachusetts Institute of Technology, Cambridge, 1996.

[37] S.C. Costa, M. Kenisarin, A review of metallic materials for latent heat thermal energy storage: Thermophysical properties, applications, and challenges, Renew. Sustain. Energy Rev. 154 (2022), 111812.
[38] U. R. W. H. An introduction to heat transfer. Oxford: Clarendon Press, 1950.
[39] D. Dropkin, E. Somerscales, Heat transfer by natural convection in liquids confined by two parallel plates which are inclined at various angles with respect to the horizontal, J. Heat Transfer 87 (1) (1965) 77–82.
[40] F. Zhou, X. Zheng, Heat transfer in tubing-casing annulus during production process of geothermal systems, J. Earth Sci. 26 (1) (2015) 116–123.
[41] M. Gonçalves, N. Simões, C. Serra, I.F. Colen, K. Rottenbacher, F.A. Almeida, Study of the edge thermal bridging effect in vacuum insulation panels: Steady and unsteady-state approaches using numerical and experimental methods, Energ. Buildings 258 (2022), 111821.